ECCOMAS Congress 2016
VII European Congress on Computational Methods in Applied Sciences and Engineering
M. Papadrakakis, V. Papadopoulos, G. Stefanou, V. Plevris (eds.)
Crete Island, Greece, 5–10 June 2016

FREE-SURFACE FLOW SIMULATIONS FOR MOORED AND FLOATING OFFSHORE PLATFORMS

Arthur E.P. Veldman[1,4], Roel Luppes[1], Peter van der Plas[1], Henri van der Heiden[1], Bülent Düz[2,3], Henk Seubers[1], Joop Helder[3], Tim Bunnik[3] and René Huijsmans[2]

[1] Institute for Mathematics and Computer Science, University of Groningen, Groningen, The e-mail: {a.e.p.veldman,r.luppes,p.van.der.plas,h.j.l.van.der.heiden,h.seubers}@rug.nl

[2] Department of Ship Hydrodynamis, Delft University of Technology, Delft, The Netherlands
e-mail: {r.h.m.huijsmans}@tudelft.nl

[3] Maritime Reseach Institute MARIN, Wageningen, The Netherlands
e-mail: {b.duz,j.helder,t.bunnik}@marin.nl

[4] Multiscale Modeling and Simulation, University of Twente, Enschede, The Netherlands

Keywords: Extreme waves, fluid–solid body interaction, CFD, local grid refinement, experimental validation.

Abstract. *During the development of the ComFLOW simulation method many challenges have to be tackled concerning the flow modelling and the numerical solution algorithm. Examples hereof are wave propagation, absorbing boundary conditions, fluid–solid body interaction, turbulence modeling and numerical efficiency. Some of these challenges will be discussed in the paper, in particular the design of absorbing boundary conditions and the numerical coupling for fluid–solid body interaction. As a demonstration of the progress made, a number of simulation results for engineering applications from the offshore industry will be presented: a wave-making oscillating buoy, a free-fall life boat dropping into wavy water, and wave impact against a semi-submersible offshore platform. For those applications, MARIN has carried out several validation experiments.*

1 INTRODUCTION

Over the centuries, understanding the motion and behavior of waves in nature has been a very popular subject among researchers from various fields of science. Even today, when we have highly capable numerical methods and computational power at our disposal, numerical modeling of water wave propagation remains a formidable challenge. During the development of the ComFLOW simulation method [1–5] many of the numerical challenges have been tackled:

- Waves should be allowed to freely enter or leave the domain, requiring absorbing or non-reflecting boundary conditions which are able to deal with the dispersive character of waves on deep water [6]. Such conditions will be discussed below in more detail.
- Accurate wave propagation requires much attention to the description (reconstruction and advection) of the free surface. Info on this aspect is to be found in the PhD thesis of Duz [7] and the forthcoming paper [8].
- The turbulence model not only has to deal with coarse grids, but should also recognize wall-bounded turbulence from free-surface turbulence. This is tackled with a new class of adaptive, minimum-dissipation turbulence LES models [9–11].
- The numerical coupling of the flow dynamics with the dynamics of a floating object has to deal with situations where the added mass is larger than the mass of the object. Hereto a more simultaneous type of numerical coupling is being developed. This paper contains more details about this issue.
- The efficiency of the simulations is enhanced by means of local grid refinement and parallelisation [12, 13].

The phenomena of interest are local but embedded in a vast spatial domain, like the interaction between free-surface waves and man-made structures. For efficient computational modeling, this spatial domain around the region of interest is truncated via artificial boundaries, leading to the fundamental question: What is the boundary condition to be imposed on these artificial boundaries in such a way that the solution in the compact domain coincides with the solution in the original domain? We thus enter the realm of absorbing boundary conditions (ABC), also known as non-reflecting, open, transparent or radiating boundary conditions. Following the pioneering research by Engquist and Majda [14], a wide variety of ABCs has been developed. These conditions not only have to be considered from a theoretical modeling point of view (well-posedness, modeling accuracy), but also from a numerical point of view (stability, numerical accuracy, efficiency). An impression of the work done thus far can be obained from several review papers [15–18]. For the work on ABCs done in the ComFLOW project we refer to the PhD theses of Wellens [19] and Düz [7]. Below we will present our latest contributions to this issue which focus on the treatment of dispersive waves, i.e. waves whose propagation speed is not known beforehand but has to be deduced from the (local) solution.

Another dimension to the above problem is added when the structures under study are moving, either free-floating or attached to a mooring system, where the interaction between the incoming waves and the dynamics of the structure comes into play. Physically, we can distinguish one-way or two-way interaction. In the former case the structure ‘simply’ reacts to the oncoming flow field. But in the latter case the interaction is such that the motion of the structure influences the flow field around the structure. The latter case also poses most challenges to the numerical coupling between flow and structure. Such a numerical coupling approach can be aggregated (monolithic) or segregated (partitioned). In the former case all discrete flow equations are combined into one single set of equations which is then solved simultaneously. In the

latter case two separate discrete systems (modules) can be recognized equipped with recipes to exchange information between the two separate modules. On the one hand this enhances the flexibility of the approach, but on the other hand it requires a (hierarchical) iterative exchange of information between the modules with its consequences for numerical stability and convergence. Below we describe our efforts to find a compromise between the robust monolithic approach and the more flexible but vulnerable partitioned approach. We will see that the ratio between the mass of the structure and its added fluid mass plays an essential role.

The organization of the paper is as follows. After an introduction of the flow equations, the new class of absorbing boundary conditions is presented. Thereafter we discuss the numerical coupling strategy between fluid and solid structure. The paper finishes with some practical applications: an oscillating buoy in a small domainn, a falling lifeboat and a semi-submersible in waves. Some of these applications are validated by experiments carried out at MARIN.

Figure 1: Drop test with free-fall lifeboat (from: www.verhoef.eu)

2 MATHEMATICAL FLOW MODEL

Incompressible, turbulent fluid flow can be modelled by means of the Navier–Stokes equations.

$$\mathcal{M}\mathbf{u} = 0, \qquad \frac{\partial \mathbf{u}}{\partial t} + \mathcal{C}(\mathbf{u})\mathbf{u} + \mathcal{G}p - \mathcal{V}\mathbf{u} = \mathbf{f}. \tag{1}$$

Here $\mathcal{M}$ is the divergence operator [1] which describes conservation of mass. Conservation of momentum is based on the convection operator $\mathcal{C}(\mathbf{u})\mathbf{v} \equiv \nabla(\mathbf{u} \otimes \mathbf{v})$, the pressure gradient operator $\mathcal{G} = \nabla$, the viscous diffusion operator $\mathcal{V}(\mathbf{u}) \equiv \nabla \cdot \nu \nabla \mathbf{u}$ and a forcing term $\mathbf{f}$. The kinematic viscosity is denoted by ν.

Turbulence is modelled by means of large-eddy simulation (LES) using a low-dissipation QR-model as formulated by Verstappen [9] and extended in the PhD thesis of Rozema [10, 11]. For its use in maritime applications, see [20, 21].

The Navier–Stokes equations (1) are discretized on an Arakawa C-grid. The second-order finite-volume discretization of the continuity equation at the 'new' time level $\cdot^{n+1}$ is given by

$$M^0 \mathbf{u}_h^{n+1} = -M^\Gamma \mathbf{u}_h^{n+1}, \tag{2}$$

[1] Calligraphic symbols denote analytic operators, whereas their discrete counterparts are denoted by upper-case italic symbols.

where M^0 acts on the interior of the domain and M^Γ acts on the boundaries of the domain. In the discretized momentum equation, convection $C(\mathbf{u}_h)$ and diffusion D are discretized explicitly in time. The pressure gradient is discretized at the new time level. In this exposition, for simplicity reasons the first-order forward Euler time integration will be used. In the actual calculations, a second-order Adams–Bashforth method is being applied.

Letting the diagonal matrix Ω denote the matrix containing the volumes of the control volumes, gives the discretized momentum equation as

$$\Omega \frac{\mathbf{u}^{n+1} - \mathbf{u}^n}{\delta t} = -C(\mathbf{u}^n)\,\mathbf{u}^n + V\mathbf{u}^n - Gp^{n+1} + \mathbf{f}. \tag{3}$$

The discrete convection operator is skew-symmetric, such that convection does not contribute to energy production or dissipation; see Verstappen and Veldman [22]. In particular, its discretization preserves the energy of the flow and does not produce artificial viscosity. To make the discretization fully energy-preserving, the discrete gradient operator and the divergence operator are each other's negative transpose, i.e. $G = -M^{0T}$, thus mimicking the analytic symmetry $\nabla = -(\nabla\cdot)^T$. In this way, also the work done by the pressure vanishes discretely.

The solution of the discrete Navier–Stokes equations is split into two steps. Firstly, an auxiliary variable $\tilde{\mathbf{u}}$ is defined through

$$\Omega \frac{\tilde{\mathbf{u}} - \mathbf{u}^n}{\delta t} = -C(\mathbf{u}^n)\,\mathbf{u}^n + D\mathbf{u}^n + \mathbf{f}. \tag{4}$$

With this abbreviation, the discrete momentum equation (3) can be reformulated as

$$\mathbf{u}^{n+1} = \tilde{\mathbf{u}} - \delta t\,\Omega^{-1} G p^{n+1}. \tag{5}$$

Secondly, by imposing discrete mass conservation (2) at the new time level, substitution of (5) results in a discrete Poisson equation for the pressure:

$$\delta t\, M^0 \Omega^{-1} G p^{n+1} = M^0 \tilde{\mathbf{u}} + M^\Gamma \mathbf{u}^{n+1}. \tag{6}$$

The liquid region and the free liquid surface are described by an improved VOF-method; see Hirt and Nichols [23] and Kleefsman et al. [1].

3 ABSORBING BOUNDARY CONDITIONS

Following the expose presentend in [7], a suitable ABC can be developed starting from the radiation condition studied by Sommerfeld [24]:

$$\frac{\partial}{\partial t}\phi + c\frac{\partial}{\partial x}\phi = 0. \tag{7}$$

This condition, formulated in the velocity potential ϕ, suppresses left-running waves at a right-hand-side boundary. Therefore, it has been proposed as a non-reflecting boundary condition by Engquist and Majda [14]. It was later extended to higher-order versions using powers of the left-hand side operator; see e.g. the review by Givoli [18].

3.1 Three dimensions

In the three-dimensional case, Higdon [25, 26] showed it possible to allow the wave under an angle of incidence α with the outflow boundary. In the higher-order conditions even more

angles can be chosen: $\alpha_p,\ p = 1, \ldots, P$, where P denotes the order:

$$\prod_{p=1}^{P} \left(\cos\alpha_p \frac{\partial}{\partial t} + c \frac{\partial}{\partial x} \right) \phi = 0. \tag{8}$$

To show the benefit of using (8) as opposed to (7), the amount of spurious reflection is investigated as a function of the angle of incidence θ. Hereto, at the artificial boundary the solution can be expressed as the sum of the outgoing and reflected waves

$$\phi(x, y, t) = e^{i(k_x x + k_y y - \omega t)} + R\, e^{i(-k_x x + k_y y - \omega t)}, \tag{9}$$

where the first term represents the wave with amplitude equal to unity impinging on the boundary, and the second term represents the spuriously reflected wave with amplitude R. The latter amplitude can be evaluated by substituting (9) into the general Higdon boundary condition (8):

$$|R_H| = \prod_{p=1}^{P} \left| \frac{\cos\alpha_p - \cos\theta}{\cos\alpha_p + \cos\theta} \right|. \tag{10}$$

Here, θ is the 'real' angle of incidence measured in the clockwise or counter-clockwise direction from the positive x-direction ($|\theta| < \pi/2$). Higdon's boundary condition (8) is non-reflecting as soon as θ equals one of the $\pm\alpha_p$'s, whereas (7) is non-reflecting for $\theta = 0$ only. A comparison of the theoretical reflection coefficients for the various ABC variants is shown in Fig. 2.

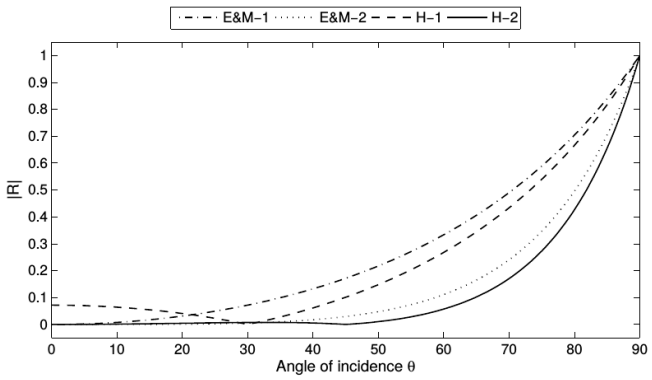

Figure 2: Reflection coefficient of four absorbing boundary conditions versus the angle of incidence θ. E&M-1 and E&M-2 stand for the 1^{st}- and 2^{nd}-order Engquist-Majda ABC. The 1^{st}- and 2^{nd}-order Higdon ABC are denoted H-1 (with $\alpha_1 = 30°$) and H-2 (with $\alpha_1 = 0°,\ \alpha_2 = 45°$), respectively [7].

For use in a Navier–Stokes context, the potential has to be related to the velocity (via the gradient of the potential) and pressure (via the dynamic free-surface condition). Doing so, it becomes a boundary condition featuring velocity and pressure. It can be embedded in the pressure Poisson equation as a boundary condition in a similar way as the substitution of (5) in (2); see also [7].

3.2 Dispersive ABC

Because of dispersion each individual wave component has its own phase speed c. Therefore, a boundary condition like (8) cannot annihilate all these wave components. We expect some amount of reflection for such a boundary condition, but it will hopefully be restricted within certain limits.

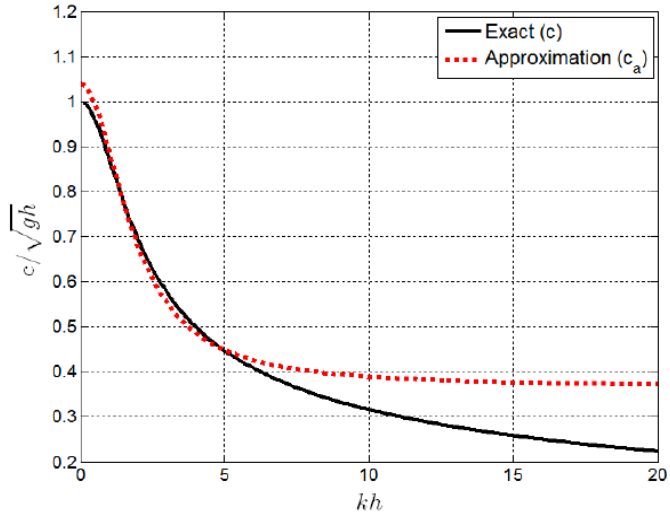

Figure 3: Padé approximation of the dispersion relation. For the coefficients in (11), $a_0 = 1.04$, $a_1 = 0.106$ and $b_1 = 0.289$ are used [7].

Firstly, we introduce a rational Padé expression which approximates the dispersion relation as

$$\text{exact: } c^2 = gh\,\frac{\tanh(kh)}{kh}; \qquad \text{approximation: } c_a = \sqrt{gh}\,\frac{a_0 + a_1(kh)^2}{1 + b_1(kh)^2}. \tag{11}$$

A proper choice of coefficients a_0 , a_1 and b_1 leads to a close approximation for the targeted range of kh values. In Fig. 3 the difference between the two curves gives an indication for the amount of reflection caused by the rational approximation. Note that the higher wave numbers will be damped by the physics of the problem, hence some reflection will disappear quickly.

A further improvement is introduced into the design of the boundary condition, by exploiting the exponential behavior of the wave potential in the z-direction. The wave number k is computed locally from the potential itself, via

$$k^2\phi = \frac{\partial^2}{\partial z^2}\phi. \tag{12}$$

This relation can be substituted into (11) and combined with (8) for $P = 1$, to reach the final form of the 1^{st}-order absorbing boundary condition ABC-1:

$$\cos\alpha\left(1 + b_1h^2\frac{\partial^2}{\partial z^2}\right)\frac{\partial\phi}{\partial t} + \sqrt{gh}\left(a_0 + a_1h^2\frac{\partial^2}{\partial z^2}\right)\frac{\partial\phi}{\partial x} = 0. \tag{13}$$

A stability analysis of this boundary condition can be found in the PhD thesis of Wellens [19].

3.3 Dispersive directional ABC

A further modification of the dispersive ABC accounts for both dispersive and directional effects of the waves. As the 2^{nd}-order Higdon ABC has superior performance over the 1^{st}-order one in terms of directional effects, we will incorporate the improvements that we made in the previous section by adding dispersive effects. As this ABC consists of the product of two operators, and considering the relations (11) and (12), we realize that only one of the operators can include the approximation for the dispersion relation. Otherwise, the product of two approximations would yield a fourth-order derivative in the z-direction which will cause difficulties

when discretized at the boundaries. Therefore, we substitute the relations (11) and (12) in only one of the two operators. The resulting expression for the 2^{nd}-order ABC-2 becomes

$$\left(\cos\alpha_1\frac{\partial}{\partial t}+c\frac{\partial}{\partial x}\right)\left[\cos\alpha_2\left(1+b_1h^2\frac{\partial^2}{\partial z^2}\right)\frac{\partial\phi}{\partial t}+\sqrt{gh}\left(a_0+a_1h^2\frac{\partial^2}{\partial z^2}\right)\frac{\partial\phi}{\partial x}\right]=0. \quad (14)$$

An in-depth analysis of the implementation and effectiveness of these boundary conditions in practical situations can be found in the PhD thesis of Duz [7, 27].

3.4 Example

As an illustration of the new type of absorbing boundary conditions we show some simulations of an oscillating sphere, with prescribed motion, producing a concentric circular wave pattern. A sphere (radius 4m) is initially located 4m above a free water surface and moves vertically along the z-direction with a sinusoidal motion $z_s(t) = 2 + 2\cos(2.4t)$. After the impact of the sphere on the water surface, a series of circular concentric waves is produced radiating outward from the center. Both ABC-1 and ABC-2 are used at the outflow boundaries and their performance in absorbing these waves is compared.

A reference solution is obtained by repeating the simulation in a large domain: see Fig. 4 for the setup of the two domains. The small domain Ω_S has $Lx_{\Omega_S} = Ly_{\Omega_S} = 50$m, its depth is $Lz_{\Omega_S} = 10$m. The larger domain Ω_L has the same depth but different length and width, $Lx_{\Omega_L} = Ly_{\Omega_L} = 400$m. The size of Ω_L is chosen in such a way that radiating circular waves do not reach the outflow boundaries of Ω_L during the simulation.

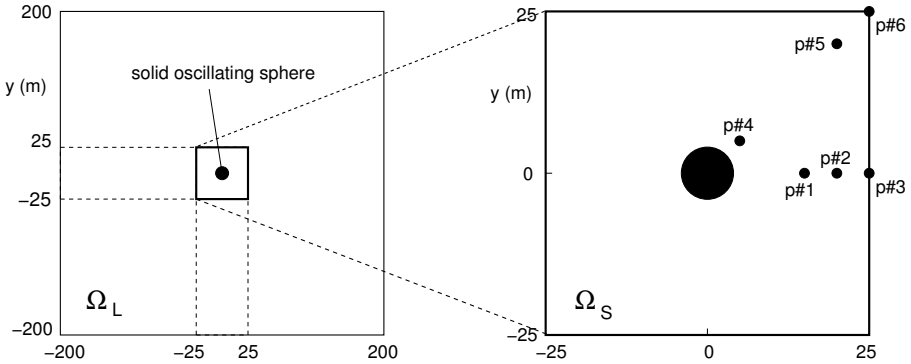

Figure 4: Setup for the test with the oscillating solid sphere showing the domain sizes (left) and the positions of the wave probes (right). The solution in Ω_L is considered as the reference solution for the solution in Ω_S.

Simulations are performed for 30s at two uniform grid resolutions of 0.25m and 0.50m. Several probes are placed in the domain to compare the free surface elevation records; see Fig. 4. Due to the prescribed motion of the sphere the generated circular wave is regular, and both the ABC-1 and ABC-2 are tuned to absorb this regular wave. But because the wave is circular, it reaches the outflow boundaries at different angles at different positions. To account for this directional effect, the angle coefficients in both boundary conditions are set to 45° (combined with 0° for the second order condition).

Figure 5 shows the free surface elevation history from the first three probes on both grid resolutions. The results in the other three probes are comparable [7]. As the circular concentric wave travels out from the center, the amplitude of the wave decreases because the energy of the wave is spread over a larger area. The probes show a significant difference between the

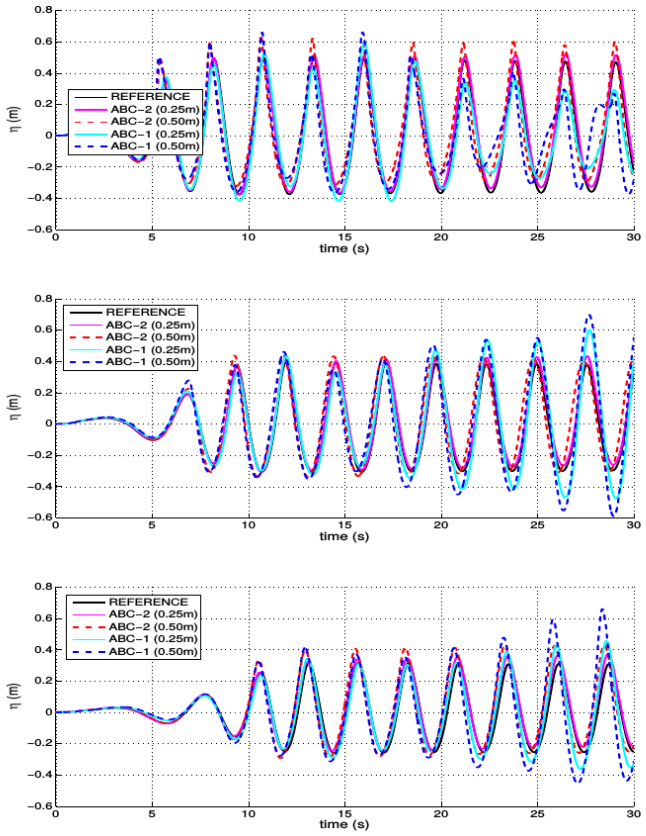

Figure 5: Free surface elevations as a function of time at various locations. From top to bottom results are shown at p#1, p#2 and p#3 [7].

performance of the ABC-1 and ABC-2, and clearly demonstrate the superiority of the ABC-2 over ABC-1.

Fig. 6 shows snapshots of the simulations at $t \approx 25$s when ABC-1 and ABC-2 are used on the fine grid. With ABC-1 different amounts of reflection at different locations result in a graphically-interesting but highly disturbed free surface. In contrast, with ABC-2 the free surface is considerably less disturbed.

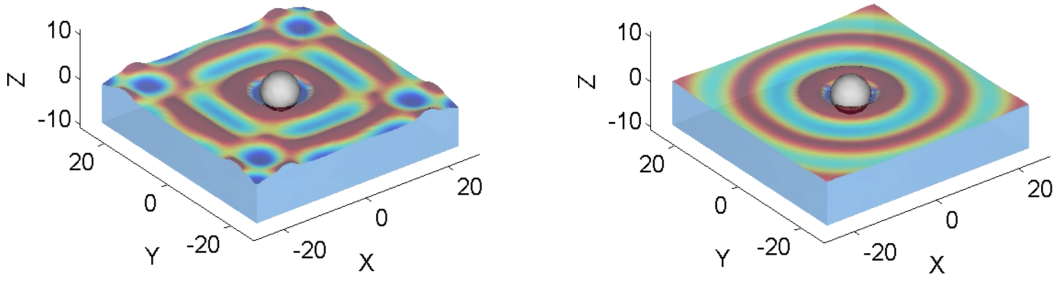

(a) ABC-1 (b) ABC-2

Figure 6: Snapshots of the simulations of an oscillating sphere at $t \approx 25$s (fine grid with resolution of 0.25m). The colors correspond with the vertical velocity at the free surface.

4 FLUID–SOLID BODY COUPLING

A further step is to allow the moving object to interact with the fluid dynamics, e.g. it is floating on the water surface. This physical two-way coupling has to be mirrorred in the numerical coupling algorithm between the flow solver and the solid-body solver. The coupling takes place along the common interface Γ between the fluid and the solid body; quantities involved are the dynamics (position and acceleration) of the solid body, and the dynamics of the fluid (in particular its pressure forces); see Fig. 7.

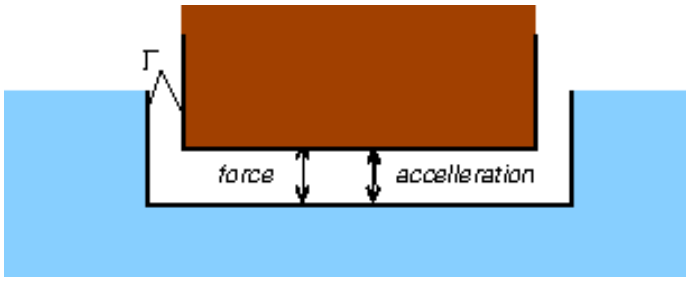

Figure 7: Schematic partitioning between fluid and solid body, with information exchange along their common interface Γ.

1. The coupling conditions at the interface between fluid and solid body basically express 'continuity' of the physics on both sides of the common interface Γ. The *kinematic* condition expresses that the boundary of the liquid region (partially) coincides with the surface of the solid body. In particular, material particles on both sides have the same velocity and acceleration (when the no-slip condition does not hold, only the normal component is continuous). Hence, it makes sense to talk about the velocity at the interface $\mathbf{u}_\Gamma$. Additionally, the *dynamic* coupling condition is based on Newton's 3^{rd} law "*action* $= -$*reaction*", which expresses equilibrium of forces. In particular, we denote the fluid pressure by p_Γ. In the sequel, we will formulate the coupled problem in terms of the two interface variables: $\mathbf{u}_\Gamma$ and p_Γ.

2. The solid-body dynamics is governed by an equation describing the accelaration $\dot{\mathbf{u}}$ of the solid body when reacting to the forces and moments $\mathbf{f}$ excerted by the fluid. The latter are found by integration of the liquid pressure over the common interface Γ. In abstract terms we denote this relation by

$$\text{solid body dynamics:} \qquad \dot{\mathbf{u}}_\Gamma = D p_\Gamma. \tag{15}$$

   The dynamics operator D involves the integration of the fluid pressure over the interface to obtain the force and moments acting on the body. Through the dynamics equations of the solid body these lead to an acceleration of the body. Thus the eigenvalues of D are inversely related to the body mass and its moments of inertia. Note that we do not show eventual external forces, as they play no essential role in the coupling algorithm.

3. The fluid dynamics governs the reaction of the fluid to the motion of the solid body. The latter creates a boundary condition along the interface Γ which has to be added to the Navier–Stokes equations (1). As a result, the pressure along the interface and acting on the solid body can be computed. In abstract notation we write

$$\text{fluid dynamics:} \qquad p_\Gamma = -M_a \dot{\mathbf{u}}_\Gamma, \tag{16}$$

where M_a is, by definition, the so-called *added mass* operator. Again, terms in $\mathbf{u}$ have been omitted because of their minor role in the analysis of the coupling process.

The above formulation (15)+(16) in principle shows two equations for the two unknowns along the interface: pressure and acceleration. Their coupling can be done in an *aggregated / monolithic* or *segregated / partitioned* way. An aggregated (or strong) coupling recombines both equations (or modules) into one single global system which is solved simultaneously. In contrast, a segregated (or weak) coupling keeps the two equations apart and solves them in an iterative way. The former approach may not always be possible, e.g. due to their 'black-box' character, or due to the large complexity of the modules; the latter approach may diverge.

4.1 Weak coupling

In practice often a segregated approach is followed. The usual way is to let the fluid determine a pressure field $p_\Gamma^{\rm old}$ which moves the solid body:

$$\dot{\mathbf{u}}_\Gamma^{\rm new} = D p_\Gamma^{\rm old}. \tag{17}$$

This motion of the solid body is then transferred to the fluid to react with a new pressure field:

$$p_\Gamma^{\rm new} = -M_a \dot{\mathbf{u}}_\Gamma^{\rm new}. \tag{18}$$

In this way, we effectively have created an iterative process

$$p_\Gamma^{\rm new} = -M_a D p_\Gamma^{\rm old}. \tag{19}$$

The iterations in such a weak coupling method will converge if and only if the spectral radius of the iteration matrix $\rho(M_a D) < 1$. Recalling that D inversely scales with the mass and inertia of the solid body, this condition becomes a requirement for the ratio between added mass and body mass. Roughly speaking, the solid body should be heavy enough. If it is not, underrelaxation can help achieving convergence, but this will require (many) additional (sub)iterations.

In practice, such iterations can be implemented as follows in the solution process for the Navier–Stokes equation (3) during the time step from $n \to n+1$. An additional subiteration process (with iteration count k) is included:

$$\text{solid-body dynamics:} \qquad (\dot{\mathbf{u}}_\Gamma^{n+1})^k = D(p_\Gamma^{n+1})^k; \tag{20}$$

$$\text{Navier–Stokes:} \qquad (p_\Gamma^{n+1})^{k+1} = M_a(\dot{\mathbf{u}}_\Gamma^{n+1})^k. \tag{21}$$

If necessary, these subiterations can be made convergent by applying (severe) underrelaxation without disturbing the time accuracy of the time integration method, but often at a considerable computational price.

Below we will demonstrate with an example of a falling life boat how many subiterations can be required. Because of this inefficiency, we would like to apply an aggregated approach (which does not require subiterations), or at least to be as close as possible to such an approach. Such an approach is the quasi-simultaneous method, originally developed for interacting aerodynamic boundary layers along airplane wings [28]; a historic overview is provided in [29, 30].

4.2 Quasi-simultaneous coupling

For iterative efficiency reasons, we would like to follow the monolithic, simultaneous approach as much as possible. With the full dynamics operator D being too complex, we look for a good approximation $\tilde{D}$ which is simple enough to be used as a boundary condition inside the Navier–Stokes solver (1). Such an approximation has been termed an *interaction law* [28–30]

$$\dot{\mathbf{u}}_\Gamma = \tilde{D} p_\Gamma. \tag{22}$$

The interaction law (22) is then incorporated in the time integration process in defect formulation:

$$\text{interaction law:} \qquad \dot{\mathbf{u}}_\Gamma^{n+1} - \tilde{D} p_\Gamma^{n+1} = (D - \tilde{D}) p_\Gamma^n \tag{23}$$

$$\text{Navier–Stokes:} \qquad p_\Gamma^{n+1} - M_a \dot{\mathbf{u}}_\Gamma^{n+1} = 0. \tag{24}$$

Another interpretation in terms of time integration is that the part $\tilde{D}$ of the dynamics equation (15) is treated implicitly and the remaining part $D - \tilde{D}$ explicitly.

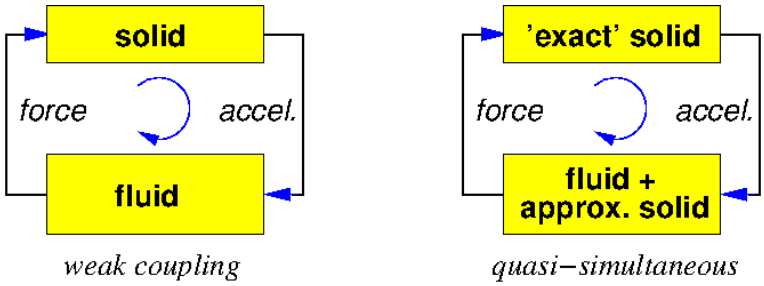

Figure 8: Weak versus quasi-simultaneous coupling.

The interaction law is a boundary condition for the Navier–Stokes equations along the interface Γ. More precisely, it will be implemented as a boundary condition for the pressure Poisson equation (6). The latter is derived by first rewriting the boundary condition (23) for $\mathbf{u}$ as

$$\mathbf{u}_\Gamma^{n+1} - \delta t \, \tilde{D} p_\Gamma^{n+1} = \mathbf{u}_\Gamma^n + \delta t \, (D - \tilde{D}) p_\Gamma^n.$$

Then the discrete momentum equation is written in the form (2), wherein the above relation is substituted through the term $M^\Gamma \mathbf{u}$. Finally a relation is obtained featuring p_Γ as a boundary condition for the Poisson equation; see also [31].

The above *quasi-simultaneous* integration can be analysed by eliminating $\dot{\mathbf{u}}$ from (23)+(24), which leads to

$$(I + M_a \tilde{D}) p_\Gamma^{n+1} = -M_a (D - \tilde{D}) p_\Gamma^n. \tag{25}$$

For $\tilde{D} \equiv 0$, we recover the iteration process (19) which breaks down when M_a is 'too large'. But with the term $M_a \tilde{D}$ on the left-hand side, it will be clear that this process will converge when $\tilde{D}$ is sufficiently close to D, in spite of a possibly 'large' M_a.

4.3 Example

To show the performance of the quasi-simultaneous approach, we now present an example of a the simulation of a life boat falling into a large breaking wave. A snapshot of the simulations

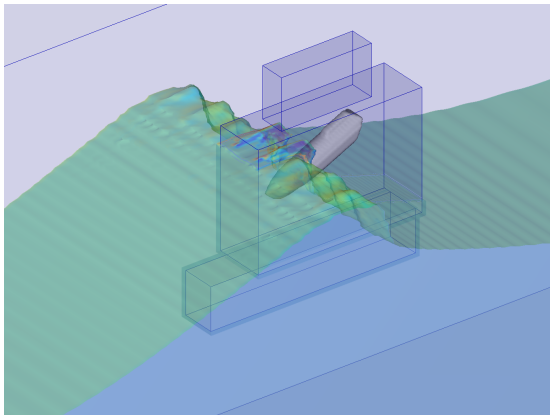

Figure 9: A snapshot of the life boat falling into a large wave. Also the locally-refined grid regions are shown.

is shown in Fig. 9. The dynamics of the life boat is modelled by means of a 6-DOF mechanical model.

The fluid flow is modelled with the Navier-Stokes equations and solved on a grid consisting of about 0.7 million active (i.e. within the fluid) grid points, with local grid refinement [12] around the life boat (Fig. 9). For physical accuracy this grid is rather coarse, but the focus in these simulations is on the numerical behaviour of the coupling process. Thus both the weak coupling procedure (19) as well as the quasi-simultaneous procedure (24) have been applied. In the latter case, the interaction law is based on the under-water part of the lifeboat (as the Poisson equation is only solved under water).

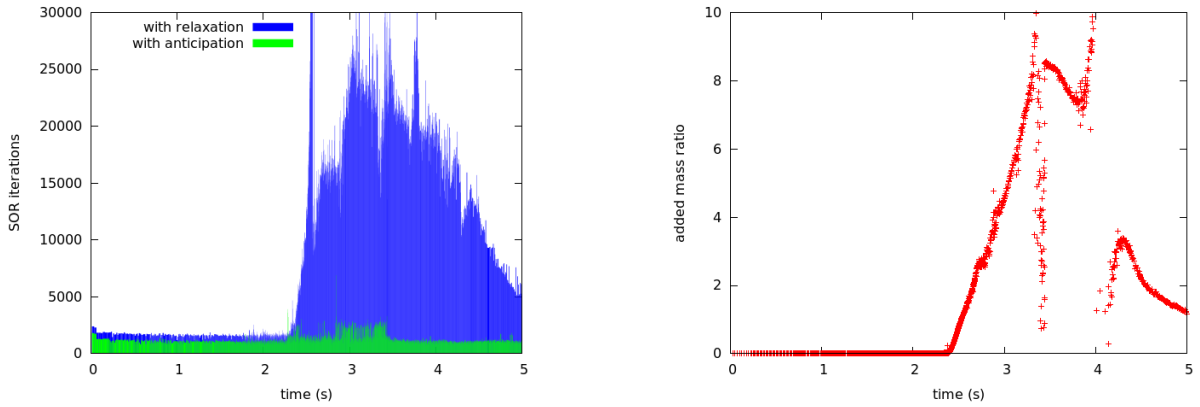

Figure 10: *Left:* The number of SOR iterations per time step for the underrelaxed weak coupling method (blue) and the anticipating quasi-simultaneous method (green)). *Right:* The estimated added mass for the falling lifeboat as a function of time. The moment of impact is clearly visible.

The most important result concerns the amount of work that is needed per time step to achieve the coupling between solid-body dynamics and fluid flow. The weak method often requires dozens of subiterations, in each of which a Poisson equation has to be solved. This number is dependent on the amount of fluid that is moved aside by the moving body, represented by the added-mass operator M_a. Fortunately, the later subiterations have a good initial guess so they are not as expensive as the earlier ones. Thus the amount of work is better represented by the total number of SOR-iterations [32] that is needed for all Poisson solves within one time step. This amount of work is shown in Fig. 10(left). The relation with the added mass becomes visible when plotting the time history of the estimated added mass in Fig. 10(right).

Comparison with Fig. 10(left) shows clearly that the number of iterations grows rapidly when the 'added-mass ratio' $\rho(DM_a)$ growths beyond 1. In contrast, the quasi-simultaneous method requires 1 or 2 subiterations (with additional Poisson solver), resulting in much less work per time step (Fig. 10).

5 WAVE IMPACT

As a third we present simulations and experiments for run-up against a semi-submersible offshore platform. The setup of the experiment, carried out at MARIN on a scale of $1:50$, is sketched in Fig. 11. A simplified semi-submersible is located in the center of the flow domain. On full scale it measures $114.5\,\text{m} \times 17.5\,\text{m} \times 28.0\,\text{m}$ with a draft of $16.0\,\text{m}$. The waves are generated by a flap-type wave generator. The basin width is $4\,\text{m}$, i.e. $200\,\text{m}$ on full scale, with solid side walls. The incoming wave has a full scale wave height of $14.7\,\text{m}$ and a wave period of $11.0\,\text{s}$. The wave elevation and pressure are measured at several positions, indicated in Fig. 11.

Figure 11: Wave run-up against a semi-submersible: snapshot of experiment (left) and position of sensors (right).

To reduce computational costs, the boundaries of the flow domain are brought closer to the structure than in the experiment, with an inflow boundary located at $240\,\text{m}$ from the center of the semi-submersible. To account for this decreased distance between the wave maker and the semi-submersible in the simulations, the incoming waves have been analyzed by wave calibration tests (without semi-submersible in the flow) [33]. The incoming computational wave thus is modeled as a 5^{th}-order Stokes wave. Note that the shape of the experimental wave differs from a theoretical Stokes wave: the wave crests can be made to correspond nicely, but a difference in the troughs is left (see Fig. 13). This has to be taken into account when comparing the simulations with the model tests.

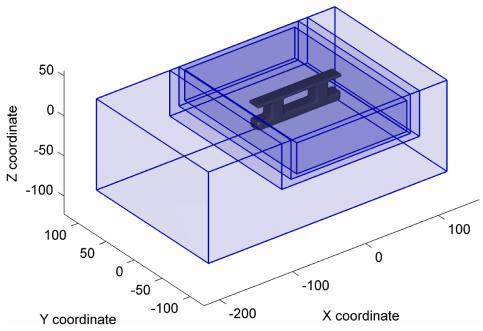

Figure 12: The grid with local refinements around the free surface and around the semi-submersible. Each box contains a refined grid level (no grid lines are shown).

The ComFLOW simulations used a one-phase flow model (as shown above) with a modern minimum-dissipation turbulence LES model [20]. Central spatial discretization with Adams-Bashforth time stepping is used throughout. The numerical simulations are shown for two different, stretched grids: $180 \times 40 \times 60 = 430$k and $360 \times 80 \times 120 = 3.5$M grid cells. The grid sizes near the semi-submersible are about 80 cm and 40 cm, respectively, in all three directions. An absorbing boundary condition, as discussed above, is applied at the outflow boundary and the simulations are carried out for several wave periods (5-10 periods, depending upon the size of the computational grid). Also results for a locally-refined grid [12, 13] are shown, with cells of around 10 m away from the structure and four refinement levels, down to 50 cm near the object, making a total of $0.5M$ cells (Fig. 12).

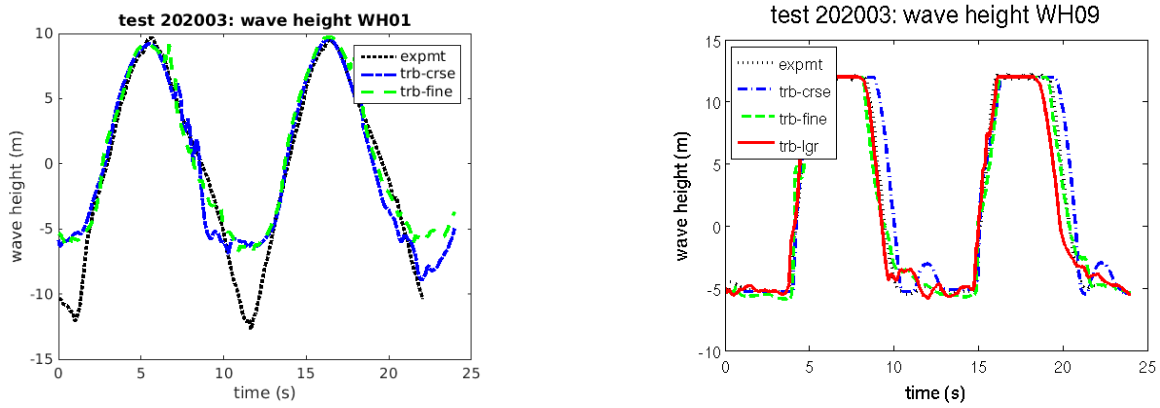

Figure 13: The wave height development in front of the semi-submersible (WH01) and at the first column (WH09) for several grids compared with experimental data.

In the presentation of results we focus on the region in front of the first column, i.e. wave-height probes WH01 and WH09, and pressure probes P11 and P15; see Fig. 11. Firstly, in Fig. 13 the wave run-up against the column is shown for the first two wave periods in the simulation. The results from the locally-refined simulation are pretty similar to those of the finest grid, although the amount of grid points is about $7\times$ less.

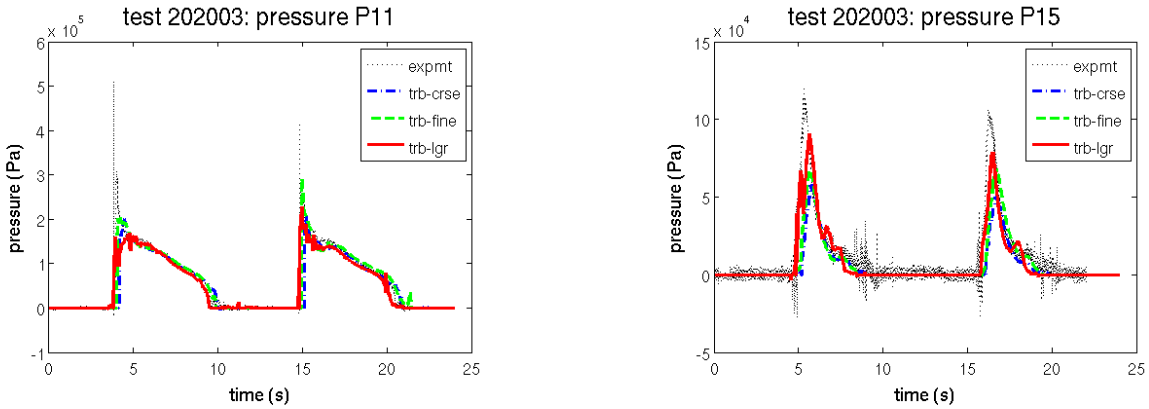

Figure 14: The pressure at the first column for several grids compared with experimental data. Left: P11 near the foot of the column; right: P15 near the top.

The pressure development near bottom (P11) and top (P15) of the first column of the semi-submersible is shown in Fig. 14. Near the top of the first column, at transducer P15, the peak

pressure values in the simulations are relatively low, which can be attributed to the limited number of grid cells along the column. The locally-refined grid, with its higher resolution near the semi-submersible, seems to catch the pressure peaks somewhat better. More detailed simulations can be found in the PhD thesis of Wemmenhove [5, 34] and the forthcoming PhD thesis of Van der Plas [12, 13].

6 CONCLUSIONS

Some recent developments in the ComFLOW simulation method have been presented. It is designed to simulate and study extreme waves and their impact on falling, floating and moored structures. Firstly, an absorbing boundary condition has been presented that adapts itself to the (local) wave number and phase speed of dispersive waves. Waves generated by an oscillating buoy show that the computational boundaries can be put close to the wave-generating object. Secondly, a life boat falling into an extreme wave reveals that the interaction between solid-body dynamics and fluid dynamics poses serious numerical challenges for their numerical coupling. It is demonstrated that a quasi-simultaneous coupling strategy can efficiently handle these challenges. Thirdly, simulations of large turbulent waves against a fixed semi-submersible, validated through experiments, demonstrate the efficiency of local grid refinement.

7 ACKNOWLEDGMENTS

The research is supported by the Dutch Technology Foundation STW, applied science division of NWO and the technology programma of the Ministry of Economic Affairs in The Netherlands (contracts 10475 and 13267).

REFERENCES

[1] K.M.T. Kleefsman, G. Fekken, A.E.P. Veldman, B. Iwanowski and B. Buchner, A Volume-of-Fluid based simulation method for wave impact problems'. *Journal of Computational Physics*, **206**, 363–393, 2005.

[2] A.E.P. Veldman, J. Gerrits, R. Luppes, J.A. Helder and J.P.B. Vreeburg, The numerical simulation of liquid sloshing on board spacecraft. *Journal of Computational Physics*, **224**, 82–99, 2007.

[3] A.E.P. Veldman, R. Luppes,T. Bunnik, R.H.M. Huijsmans, B. Düz, B. Iwanowski, R. Wemmenhove, M.J.A. Borsboom, P.R. Wellens, H.J.L. van der Heiden and P. van der Plas (2011). Extreme wave impact on offshore platforms and coastal constructions'. *Proceedings 30th Conference on Ocean, Offshore and Arctic Engineering OMAE2011*, Rotterdam (The Netherlands), 19–24 June, 2011, paper OMAE2011-49488.

[4] A.E.P. Veldman, R. Luppes, H.J.L. van der Heiden, P. van der Plas, B. Düz and R.H.M. Huijsmans (2014). Turbulence modeling, local grid refinement and absorbing boundary conditions for free-surface flow simulations in offshore applications. *Proceedings 33rd International Conference on Ocean, Offshore and Arctic Engineering*, San Francisco (USA), 8–13 June, 2014, paper OMAE2014-24427.

[5] R. Wemmenhove, R. Luppes, A.E.P. Veldman and T. Bunnik, Numerical simulation of hydrodynamic wave loading by a compressible two-phase flow method. *Computers and Fluids*, **114**, 218–231, 2015 (doi: 10.1016/j.compfluid.2015.03.007).

[6] B. Düz, R.H.M. Huijsmans, A.E.P. Veldman, M. Borsboom and P. Wellens, An absorbing boundary condition for regular and irregular wave simulations. In: L. Eça, E. Oñate, J. Garçia-Espinosa, T. Kvamsdal and P. Bergan (Eds.), *Computational Methods in Applied Sciences*, **29**, Springer, 2014.

[7] B. Düz, *Wave generation, propagation and absorption in CFD simulations of free surface flows.* PhD thesis, Technical University Delft, 2015.

[8] B. Düz, M.J.A. Borsboom, A.E.P. Veldman, P.R. Wellens, R.H.M. Huijsmans, The effect of different volume-of-fluid (VOF) methods on energy dissipation in simulations of propagating water waves. In preparation.

[9] R.W.C.P. Verstappen, When does eddy viscosity damp subfilter scales sufficiently? *Journal of Scientific Computing*, **49**, 94–110, 2011.

[10] W. Rozema, *Low-dissipation methods and models for the simulation of turbulent subsonic flow.* PhD thesis, University of Groningen, 2015.

[11] W. Rozema, H.J. Bae, P. Moin and R. Verstappen, Minimum-dissipation models for large-eddy simulation. *Physics of Fluids* **27**, 085107, 2015.

[12] P. van der Plas, A.E.P. Veldman, H.J.L. van der Heiden and R. Luppes, Adaptive grid refinement for free-surface flow simulations in offshore applications. *Proceedings 34th International Conference on Ocean, Offshore and Arctic Engineering OMAE2015*, St. John's (Canada), 31 May–5 June, 2015, paper OMAE2015-42029.

[13] P. van der Plas, *Local grid refinement for free-surface flow simulations.* PhD thesis, University of Groningen, 2016.

[14] B. Engquist and A. Majda, Absorbing boundary conditions for the numerical simulation of waves". *Mathematics of Computation*, **31**, 629–651, 1977.

[15] D. Givoli, Non-reflecting boundary conditions. *Journal of Computational Physics*, **94**, 1–29, 1991.

[16] S. Tsynkov, Numerical solution of problems on unbounded domains. a review. *Applied Numerical Mathematics*, **27**, 465–532, 1998.

[17] T. Hagstrom, Radiation boundary conditions for the numerical simulation of waves. *Acta Numerica*, **8**, 47–106, 1999.

[18] D. Givoli, High-order local non-reflecting boundary conditions: a review. *Wave Motion*, **39**, 319–326, 2004.

[19] P. Wellens, *Wave simulation in truncated domains for offshore applications*. PhD thesis, Delft University of Technology, 2012.

[20] H.J.L. van der Heiden, A.E.P. Veldman, R. Luppes, P. van der Plas, J. Helder and T. Bunnik, Turbulence modeling for free-surface flow simulations in offshore applications. *Proceedings 34th International Conference on Ocean, Offshore and Arctic Engineering OMAE2015*, St. John's (Canada), 31 May–5 June, 2015, paper OMAE2015-41078.

[21] A.E.P. Veldman, R. Luppes, P. van der Plas, H.J.L. van der Heiden, J. Helder and T. Bunnik (2015). Turbulence modeling for locally-refined free-surface flow simulations in offshore applications. *Proceedings Int Symp Offshore and Polar Eng ISOPE2015*, Kona (Hawaii, USA), 23-27 June, 2015, paper 2015-TPC-0282.

[22] R.W.C.P. Verstappen and A.E.P. Veldman, Symmetry-preserving discretization of turbulent flow. *Journal of Computational Physics*, **187**, 343–368, 2003.

[23] C.R. Hirt and B.D. Nichols, Volume of fluid (VOF) method for the dynamics of free boundaries. *Journal of Computational Physics*, **39**, 201–225, 1981.

[24] A. Sommerfeld, *Partial differential equations in physics*. Academic Press, 1949.

[25] R. Higdon, Absorbing boundary conditions for difference approximations to the multi-dimensional wave equation. *Mathematics of Computation*. **47**, 437–459, 1986.

[26] R. Higdon, Numerical absorbing boundary conditions for the wave equation. *Mathematics of Computation*, **49**, 65–90, 1987.

[27] B. Düz, M.J.A. Borsboom, P.R. Wellens, A.E.P. Veldman, R.H.M. Huijsmans, An absorbing boundary condition for free-surface water waves. In preparation.

[28] A.E.P. Veldman, New quasi-simultaneous method to calculate interacting boundary layers. *AIAA Journal*, **19**, 79–85, 1981.

[29] A.E.P. Veldman, Matched asymptotic expansions and the numerical treatment of viscous-inviscid interaction. *Journal of Engineering Mathematics*, **39**, 189–206, 2001.

[30] A.E.P. Veldman, A simple interaction law for viscous-inviscid interaction. *Journal of Engineering Mathematics*, **65**, 367–383, 2009 (doi: 10.1007/s10665-009-9320-0).

[31] A.E.P. Veldman, Missing boundary conditions? discretize first, substitute next, combine later. *SIAM Journal of Scientific and Statistical Computing,*. **11**, 82–91, 1990.

[32] E.F.F. Botta and M. Ellenbroek, A modified sor method for the poisson equation in unsteady free-surface flow calculations. *Journal of Computational Physics*, **60**, 119–134. 1985.

[33] B. Iwanowski, M. Lefranc and R. Wemmenhove, CFD simulation of wave run-up on a semi-submersible and comparison with experiment.*Proceedings 28th Conference on Ocean, Offshore and Arctic Engineering OMAE2009*, Honolulu (USA), 31 May–5 June, 2009, paper OMAE2009-79052.

[34] R. Wemmenhove, *Numerical simulation of two-phase flow in offshore environments*. PhD thesis, University of Groningen, 2008.